Transition metal doped α-MnO₂ nanorods as bifunctional catalysts for efficient oxygen reduction and evolution reactions

Mechthild Lübke,[a,b] Afriyanti Sumboja,[b] Liam McCafferty,[a] Ceilidh F. Armer,[b,c] Albertus D. Handoko,[b] Yonghua Du,[d] Kit McColl,[a] Furio Cora,[a] Dan Brett,[e] Zhaolin Liu,[b] Jawwad A. Darr*[a]

Abstract: Nano-sized α-MnO₂ nanorods doped with Co or Ru were directly synthesized using a one step and scalable continuous hydrothermal process (production rate herein 10 g h⁻¹) and investigated as inexpensive bifunctional catalysts for both Oxygen Reduction Reaction (ORR) and Oxygen Evolution Reaction (OER) for rechargeable Zn-air batteries application. The extensive material characterizations were complimented with density functional theory studies and extended X-Ray absorption fine structure (EXAFS) spectroscopy measurements in order to describe the roles of the dopants in the α-MnO₂ structure. Electrochemical ORR and OER investigations of the as-prepared doped α-MnO₂ nanomaterials were compared to more conventional and expensive Pt/C or RuO₂ catalyst. The doped manganese oxide nanomaterials were used as catalysts for the positive electrode in zinc air batteries and displayed excellent performance (overpotential was 0.77 and 0.68 V for α-MnO₂ modified with 7.6 at% Co and 9.4 at% Ru, respectively). Overall, this study investigates the rationale behind the improved bifunctional catalytic activities of the doped metal oxides catalysts and their corresponding physical properties.
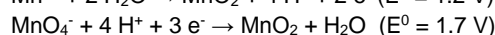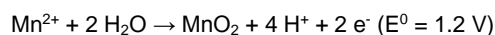
Introduction

Electrochemical Oxygen Reduction Reactions (ORRs) and Oxygen Evolution Reactions (OERs) are important in the fields of electrochemical energy storage and conversion, with applications including fuel cells,[1] electrolysers[2] and metal air batteries.[3] In a metal air battery, O₂ is the active medium at the positive electrode, where OER and ORR occur during charging and discharging, respectively. The sluggish kinetics of OER and/or ORR, require a significant overpotential to drive the reactions, which is detrimental to round-trip efficiency.[4] Furthermore, many current catalysts are based on rather large amounts of expensive and precious metals, e.g. Pt/C or Pt-alloys for ORR and Ru-based materials such as RuO₂, as the most effective OER catalysts.[3a, 5] Thus, there is interest in developing more sustainable and inexpensive elements for either OER or ORR reactions, but also in the possibility of using bifunctional catalysts that can catalyze both.

Amongst candidate sustainable catalyst replacements for Pt or Ru oxide, the α-MnO₂ phase has been shown to be a better ORR (and potentially OER) catalyst, compared to the other MnO₂ phases (e.g. β-, γ- or δ-MnO₂).[6] Both the precursors and synthesis methods are relatively inexpensive, which suggests this material is a sustainable replacement for the Pt or Ru-based benchmark materials.[7] Nanosized particles (high surface area) are crucial for high-performance OER and ORR catalysts, due to the high accessibility of water molecules towards the catalysts and high ionic conductivities.[6a] For improved OER and ORR catalyst performance, several dopants have previously been doped into α-MnO₂, e.g. Fe, Co, Ni, Ti and Cu.[6a, 8] In particular, the OER performance of α-MnO₂, still needs further improvements from that currently reported to date. An approach to improve this might be to dope known OER oxide catalyst transition metals into α-MnO₂, namely cobalt[9] or ruthenium.[3a, 5] Several groups have shown the synergistic and advantageous performance of bifunctional catalysts composed of mixed cobalt-manganese oxides[9b, 9d, 10] and mixed ruthenium-manganese oxides.[11] Despite this, doping and simultaneous nano-sizing of α-MnO₂ (using scalable methods) towards improved OER performance, has not been intensively studied.

Herein, the direct and scalable synthesis of doped α-MnO₂ was performed using a doped hydrothermal, comproportionation reaction, similar to that first reported by Wang et al.[12] Two manganese salts containing Mn²⁺ and Mn⁷⁺, were used as precursor solutions in the appropriate ratio, resulting in an average oxidation state of Mn⁴⁺ in the product. This reaction is comprised of two half-reactions[12]:

$$Mn^{2+} + 2\ H_2O \rightarrow MnO_2 + 4\ H^+ + 2\ e^-\ (E^0 = 1.2\ V)$$
$$MnO_4^- + 4\ H^+ + 3\ e^- \rightarrow MnO_2 + H_2O\ (E^0 = 1.7\ V)$$

In the current study, nanosized α-MnO₂ based powders were directly synthesized using a laboratory scale (<10 g per hour production rate) continuous hydrothermal flow synthesis (CHFS) reactor. This synthesis method has already been developed at the lab-scale and pilot plant scale (production rates of up to 2 kg per hour) by the authors.[13] The CHFS process is a green, rapid and continuous process that mixes supercritical water (in an engineered mixer) with appropriate metal salts in ambient

[a] M. Lübke, Dr. L. McCafferty, K. McColl, Prof. Dr. F. Cora, Prof. J. A. Darr*
Department of Chemistry
University College London
20 Gordon Street, London, WC1H 0AJ, UK
*E-mail: j.a.darr@ucl.ac.uk

[b] M.Lübke, Dr. A. Sumboja, C.F. Armer, Dr. A.D. Handoko, Dr. Z. Liu
Institute of Materials Research and Engineering (IMRE)
A*STAR (Agency for Science, Technology and Research)
2 Fusionopolis Way, Innovis #08-03, Singapore 138634

[c] C.F. Armer
College of Engineering and Computer Science
Australian National University
Canberra, ACT 0200, Australia

[d] Dr. Y. Du
Institute of Chemical & Engineering Sciences
A*STAR, (Agency for Science, Technology and Research)
1 Pesek Road, Jurong Island, Singapore 627833

[e] Prof. D.J. Brett
Electrochemical Innovation Lab
Department of Chemical Engineering
University College London
Torrington Place, WC1E 7JE, UK

Supporting information for this article is given via a link at the end of the document.

temperature water, to instantly form nanoparticles of the corresponding metal oxides (*via* a rapid hydrolysis, decomposition and dehydration reactions) which are collected downstream after cooling in-flow within the process.[14] The CHFS process is described in more detail in the experimental section (and supplementary information, Figure S1) and is suitable for the production of high surface area and small particle size products (including ORR and OER catalysts). Consequently, the small size of these materials, may be useful to improve charge transfer and transport processes.[15]

The primary aim of this report was to identify more sustainable and inexpensive alternatives to Pt/C or Ru oxide based catalysts that are capable of displaying both ORR and OER performance. Therefore, the electrochemical properties of doped α-MnO_2 nanomaterials (with <8 at% Co or <10 at% Ru content), were initially investigated in terms of their electrochemical ORR and OER performances using rotating disk electrode experiments. All materials were compared with a Pt/C (benchmark for ORR) and RuO_2 (benchmark for OER) catalysts, and the most promising materials were evaluated as bifunctional catalysts for the positive electrode of Zn-air batteries (vs Zn metal).

Results and Discussion

Materials Characterization

All materials were labeled according to the dopant amount from elemental analyses (XRF) rather than the nominal values used in the CHFS precursors, *e.g.* MnO_2-4.8%Ru refers to a ruthenium content of 4.8 at% of Ru in the α-MnO_2 based sample. All materials were collected as black powders with yields >90 % (production rate *ca.* 10 g.h^{-1}).

TEM images revealed 1D single-crystal nanorods as the main particle morphology for all samples (Figure 1). All particles showed high crystallinity as evidenced by the presence of lattice fringes with lattice spacing of 0.31 nm, which is
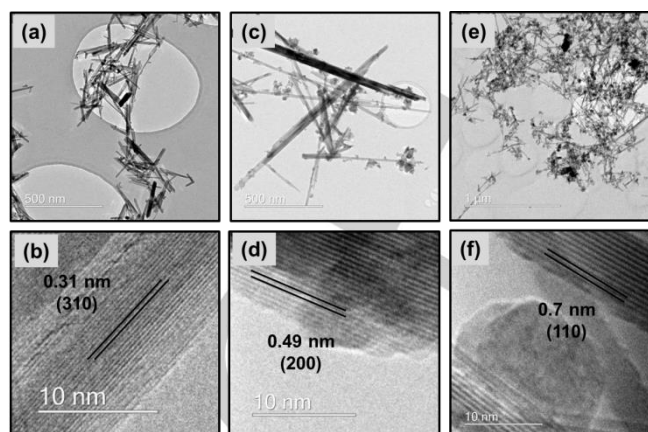

Figure 1. TEM images of a-b) MnO_2, c-d) MnO_2-7.6%Co, e-f) MnO_2-9.4%Ru.

consistent with the (310) plane of α-MnO_2, Figure 1a,b. Pristine MnO_2 particles showed an average length of *ca.* 200 nm. Adding Co^{2+} or Ru^{3+} salts to the Mn precursor salts, resulted in differing particle morphologies in the CHFS process. Nanorods and spherical particles were present in each doped sample (Figure 1c,d for MnO_2-7.6%Co and Figure 1e,f for MnO_2-9.4%Ru). The nanorods were drastically bigger for sample MnO_2-7.6%Co (*ca.* 700 nm length) compared to MnO_2-9.4%Ru (range of *ca.* 200 to 400 nm in length). More TEM images can be found in supplementary Figure S2. Additional SEM images revealed that a representative particle size distribution was measured *via* TEM (supplementary Figure S3).

The BET specific surface area was 72.7 m^2.g^{-1} for undoped MnO_2 and *ca.* 38.1 and 49.4 m^2.g^{-1} for samples MnO_2-2.9%Co and MnO_2-7.6%Co, respectively. In contrast, when a Ru^{3+} salt was added into the precursor solution, the resulting nanomaterials had a surface area of 71.0 and 87.4 m^2.g^{-1} for MnO_2-4.8%Ru and MnO_2-9.4%Ru samples, respectively.
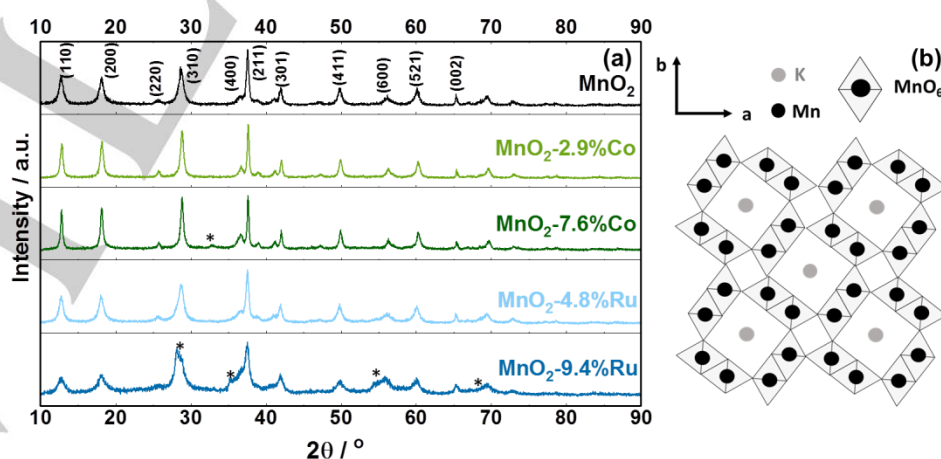

Figure 2. (a) XRD patterns (Cu-source) of all synthesized samples, the included star (*) indicates the secondary minor impurity peak positions for the samples MnO_2-7.6%Co and MnO_2-9.4%Ru. (b) Square tunnel structure of α-MnO_2 emphasizing the (partially) location of K^+ as a stabilizing cation.

Table 1. Materials characterizations: (a) refined cell parameters; (b) atomic ratio of Mn to K obtained from XRF; (c) Mn3s peak splitting obtained from XPS; (d) BET surface area.

Sample	a				b	c	d
	a / Å	c / Å	Unit cell Volume / Å^3	R_{wp} / %	Atomic ratio / % Mn:K	Mn3s peak splitting / eV	BET surface area / m^2 g^{-1}
MnO$_2$	9.847(1)	2.8580(4)	277.14(7)	15.12	93.52:6.48	4.53	72.7
MnO$_2$-2.9%Co	9.8226(9)	2.8565(3)	275.60(6)	16.60	92.78:7.22	4.50	38.1
MnO$_2$-7.6%Co	9.8087(9)	2.8567(3)	274.85(6)	14.48	94.05:5.95	4.73	49.4
MnO$_2$-4.8%Ru	9.847(1)	2.8620(5)	277.51(7)	14.81	93.18:6.82	4.50	71.0
MnO$_2$-9.4%Ru	9.847(3)	2.864(1)	277.7(2)	15.53	95.51:4.49	4.55	87.4

The diffraction data of all materials can be matched to the tetragonal α-MnO$_2$ as the main phase (space group I 4/m, No. 83, Figure 2a). The best Rietveld refinement fit for the α-MnO$_2$ samples was found to be the hollandite type structure with the empirical formula of K$_{2-x}$Mn$_8$O$_{16}$•nH$_2$O (ICSD 59159) where K$^+$ (and/or H$_2$O) is incorporated into some of the 2×2 MnO$_6$ tunnel structure, see Figure 2b. Although hydrated α-MnO$_2$ can be stable without any cations, the incorporation of K$^+$ within the 2×2 MnO$_6$ tunnel is commonly seen in α-MnO$_2$ synthesized using KMnO$_4$ as a precursor and is known to significantly improve its stability.[6a] The major difference compared to the reference XRD patterns was that the (211) and (002) peaks of all as-synthesized materials, showed higher relative intensities compared to the ICSD reference (see also supplementary Figure S4);[16] several reports have addressed reasons for these differences.[17] Li *et al.* ascribed this phenomenon to the (210) planes being aligned to the side walls.[16a, 16b] Simply described, the *c*-channels grow parallel to the nanorod axis (see TEM images with strongly detected lattices in the ab-plane, Figure 1).

Rietveld refinement results are shown in Table 2. Due to the orientation of the particles, a proper fit was challenging, which was also noted by Li *et al.* (weighted profile R-factor, R_{wp}: 13.50).[16b] Refinement of the XRD patterns revealed a decrease in the *a* and *b* directions for the samples with cobalt and a slight increase for ruthenium doping, compared to undoped α-MnO$_2$. The *c* direction increased for Ru-doping and decreased for Co-doping compared to α-MnO$_2$. This matched the unit cell volumes with a decrease with Co-doping and an increase with Ru-doping. The cationic radii in an octahedral environment for Mn^{4+}, Co^{2+}, Co^{3+} and Ru^{4+} are 67, 79, 68.5 and 76 pm, respectively. As the possible dopants had larger cationic radii than Mn^{4+}, a unit cell volume increase might have been expected for Co$^{2+/3+}$ doping. Duan *et al.* conducted theoretical investigations on the effects of Fe^{3+} (69 pm) doping on the structure of α-MnO$_2$ and suggested a significant contraction of the doped FeO$_6$ octahedra compared to the MnO$_6$ octahedra, would lead to a reduction in the average M–O bond

length.[18] Sample MnO$_2$-9.4%Ru showed a minor rutile RuO$_2$ secondary phase (similar to the reference pattern ICSD 15071, supplementary Figure S4), and sample MnO$_2$-7.6%Co showed a very small impurity in the XRD pattern at 2θ = 14.9° (Figure 2a), but the intensity was very low indeed. No other impurities were observable in the other samples *via* XRD. XRF determined that the added transition metals were present in the final product. In addition to the transition metals, some potassium was detected for all samples (Table 1).

Investigation of Mn 3s spin-orbit splitting for each sample reveals the ratio of Mn^{3+} and Mn^{4+} at the surface of the sample.[19] A splitting of 4.6±0.1 eV is indicative of Mn^{4+} and 5.2±0.1 eV for Mn^{3+}.[20] All samples showed a spin-orbit splitting in the range 4.6±0.1 eV and therefore in the 4+ state (Figure 3a).

Co 2p splitting energies are plotted in Figure 3b for sample MnO$_2$-7.6%Co. The core level Co 2p$_{3/2}$ signal was convoluted to four fitted peaks with binding energies (BEs) of 780.0 and 785.9 eV, which could be assigned to Co^{3+} and its satellite line and the other couple at a higher BE (781.6 and 789.5 eV) could
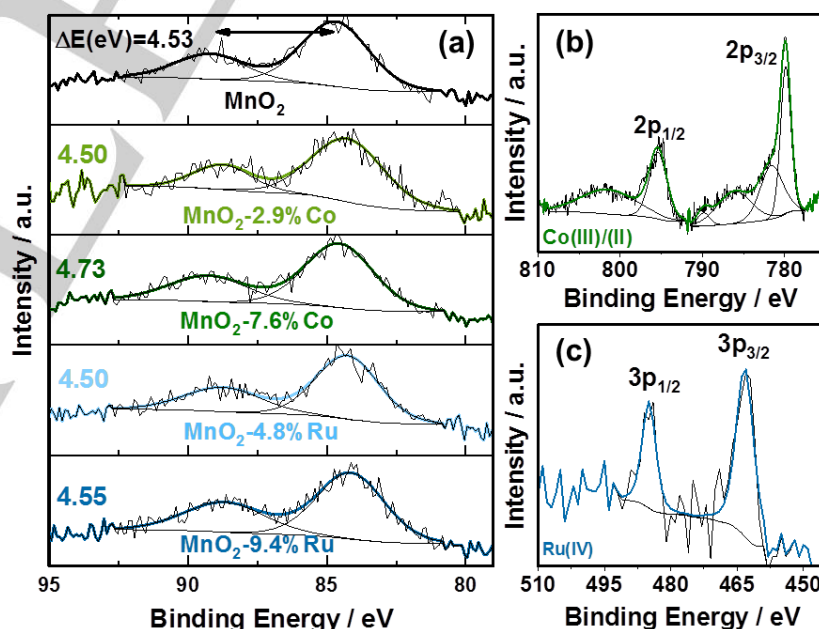

Figure 3. High-resolution XPS spectra with splitting energies of (a) Mn 3s, (b) Co 2p for sample MnO$_2$-7.6%Co and (c) Ru 3p for sample MnO$_2$-9.4%Ru.

be assigned to Co²⁺ and its respective satellite line.[21] The BE value with a spin–orbit splitting of *ca.* 15.5 eV (795.4 eV Co 2p₁/₂ and 779.9 eV in the Co 2p₃/₂) indicated that the Co³⁺ species are largely on the surface.[22] Using the Shirley method to calculate the exact Co²⁺ to Co³⁺ ratio, suggested a value of *ca.* 2:3,[23] (for additional XPS data for sample MnO₂-2.9%Co see supplementary Figure S5). Ru 3p splitting energies are plotted in Figure 3c for sample MnO₂-9.4%Ru. The BE value with a spin–orbit splitting of *ca.* 21.7 eV (484.9 eV Ru 3p₁/₂ and 463.2 eV in the Ru 3p₃/₂) indicated that the Ru⁴⁺ species are predominant on the surface.[24]
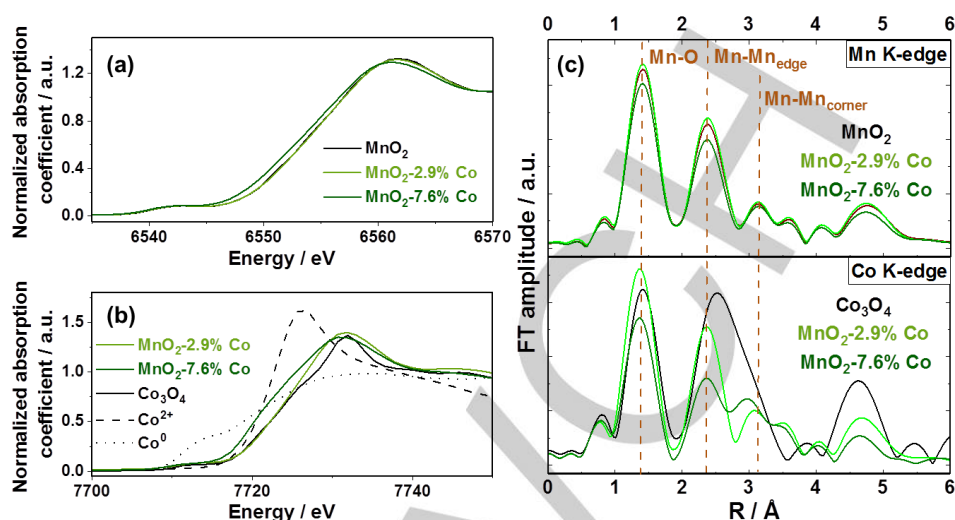

Figure 4. Normalized XANES of different cobalt-doped samples compared to undoped MnO₂ for determination of the (a) Co- and (b) Mn-oxidation state. (c) FT data of Mn-K-edge and Co-K-edge without phase correction.

In order to further evaluate the oxidation states in the cobalt based samples compared to MnO₂, X-ray absorption spectroscopy (XAS) measurements were performed, Figure 4a,b. The normalized Co-K-edge X-ray absorption near edge structure (XANES) spectra are presented in Figure 4a. The standard samples of Co⁰, Co²⁺ and Co₃O₄, were used to confirm the oxidation states. The sample MnO₂-2.9%Co had more Co³⁺ compared to sample MnO₂-7.6%Co, as the former had similar valence with Co₃O₄, *i.e.* a ratio of 2+ to 3+ of 1:2 (Shirley method from XPS showed ratio of 2:3). The normalized Mn-K-edge XANES spectra are presented in Figure 4b, and showed Mn⁴⁺ as main oxidation state for all samples, with slightly lower oxidation state for MnO₂-7.6%Co (similar to the results obtained from XPS).

In order to determine the local structural parameters of phase pure α-MnO₂ and the Co-doped MnO₂, Fourier-transformed (FT) magnitudes of k³-weighted extended X-Ray absorption fine structure (EXAFS) spectroscopy, were obtained; see Figure 4c. The Mn-K-edge revealed distinct FT peaks within 3.50 Å range and showed the typical α-MnO₂ features with a (2×2) tunnel structure. The strongest peak at 1.45 Å was the Mn-O bond in the MnO₆ octahedra. The second (2.48 Å) and third peaks (3.13 Å) were assigned to the edge-sharing (Mn-Mn_edge) and corner-sharing (Mn-Mn_corner) MnO₆ octahedra. Sample MnO₂-7.6%Co showed a slight distortion for the Mn-Mn_edge peak. For the Co-K-edge, distinct FT peaks showed that the majority of the Co ions were successfully doped into the α-MnO₂ structure for each sample because their peak/reflection shape was more similar to MnO₂ rather than that of Co₃O₄. For the higher Co-loading sample, the neighboring atoms were slightly distorted, which might also explain the detected additional phase from XRD. Lee *et al.* reported that for higher concentrations of Co²⁺/³⁺ in α-MnO₂, a shift towards δ-MnO₂ occurred.[25] Since the Mn-K-edge

showed distinct FT peaks of α-MnO₂, the secondary phase might be related to a cobalt compound.

To investigate the location of the ruthenium component in the Ru-doped MnO₂, periodic density functional theory (DFT) calculations using the hybrid-exchange B3LYP functional were performed on MnO₂ polymorphs (α- and β-) substituted with Ru. For full details of the calculations, see the experimental part and supplementary information. Ru incorporation in MnO₂ is relatively straightforward to investigate computationally, since no charge balancing is required when Mn⁴⁺ is replaced by Ru⁴⁺. Investigating the location of Co incorporation into α-MnO₂ using DFT, would require a full defect characterization study, including varying oxygen vacancy concentration to retain charge neutrality when Mn⁴⁺ is replaced by Co²⁺/³⁺. As we can clearly see that Co incorporation is occurring from Co-K edge EXAFS, DFT studies were only applied for Ru⁴⁺ substitution. Calculations on the (rutile) β-MnO₂ polymorph were included since RuO₂ only forms the rutile crystal structure. Thus, Ru⁴⁺ might be expected to substitute more favorably into a MnO₂ polymorph that it shares a structure with, which could in turn have implications for the synthesis products.

β-MnO₂ is known to be the experimental ground state of pristine MnO₂, however, precise comparisons of formation energy between the MnO₂ polymorphs is challenging experimentally since stability can be influenced by hydration levels and the incorporation of ions in the channels.[26] For example, α-MnO₂ can be stabilized by >40 kJ mol⁻¹ relative to β-MnO₂ depending on K⁺ ion incorporation and hydration.[26] Furthermore, the accurate determination of relative stabilities of many crystalline polymorphs including MnO₂ is a well-known challenge for DFT.[27] The ordering of experimental stability of the pristine polymorphs is correctly reproduced by the calculations reported

herein, which show that β- is more stable than α- by 17.4 kJ mol^{-1}.

Defect formation energies in the 16 cation supercells (6.25 % concentration Ru) were determined relative to the energy of the relevant polymorph by the following calculation:

$$\Delta E_{sub} = E(Mn_{15}RuO_{32}) - 15 \times E(MnO_2) - E(RuO_2)$$

Our calculations find that the defect formation energy for the incorporation of Ru^{4+} into α-MnO_2 is +0.92 eV / unit cell [0.068 eV / formula unit (f.u.) MnO_2, or 6.5 kJ mol^{-1}], whereas in β-MnO_2 it is +0.25 eV / unit cell (0.016 eV / f.u. MnO_2 or 1.5 kJ mol^{-1}).

The destabilization of α-MnO_2 relative to β-MnO_2 with the incorporation of Ru^{4+} of the order of +5 kJ mol^{-1}, may have implications for the synthesis products. These results may explain the observation of an impurity rutile phase in the MnO_2-9.4%Ru sample (Figure 2), which could be attributed to the formation of RuO_2 (identified *via* XRD) or more likely a mixed rutile material with stoichiometry $Ru_xMn_{(1-x)}O_2$, similar to the results of Xu *et. al.*[28] However, the authors note that despite the higher thermodynamic Ru defect formation energy in α-MnO_2, a low concentration of Ru^{4+} substitution into α-MnO_2 cannot be excluded. The CHFS synthesis method employed produces a kinetic rather than thermodynamic product, and CHFS has been shown to increase the solid-solution solubility[29] of metal oxides beyond what is generally achieved in conventional solid-state or batch hydrothermal syntheses. The calculated lattice parameters of Ru-substituted α-MnO_2 (Table S2) are consistent with the small unit cell expansion observed for the experimental XRD (Table 1).

To understand the electronic effects that might occur with Ru substitution into MnO_2, the band structure of pristine and Ru-doped α- and β- polymorphs of MnO_2 were investigated. The bandgap of pristine α-MnO_2 is found by B3LYP to be 2.96 eV. The substitution of Ru^{4+} at a nominal concentration of 6.25 %, closes the bandgap to 1.8 eV, and Ru 4d states form the top of the valence band (VB) and bottom of the conduction band (CB) (supplementary Figure S6). Ru substitution into β-MnO_2 is also shown to close the bandgap, from 1.8 eV (pristine β-MnO_2) to 1.4 eV (Ru-substituted β-MnO_2), and the Ru 4d states form the top of the VB and bottom of the CB, as they do in Ru-substituted α-MnO_2. We would therefore expect that in both MnO_2 polymorphs, Ru substitution would contribute to improved electronic conductivity, and Ru atoms would provide electroactive sites for electron transfer for the OER and ORR.

To summarize, all samples showed α-MnO_2 as the main phase and 1D single-crystal nanorods as the main particle morphology, with the rods oriented along the *c*-channels. Addition of Co^{2+} in the precursor solution during synthesis, resulted in bigger nanorods and lower surface area. Moreover, the unit cell volume decreased. XAS measurements confirmed the successful incorporation of the Co atom in the Mn position. Addition of Ru^{4+} precursor solution during synthesis resulted in higher surface

area with a secondary spherical rutile RuO_2 or Ru-incorporated β-MnO_2 phase for higher Ru concentration combined with doping into α-MnO_2. The successful doping of some of the Ru was confirmed *via* a change in the lattice parameters and suggested *via* DFT studies. Ru-doping into α-MnO_2 (and β-MnO_2) is expected to increase the electronic conductivity.

Electrochemical Characterization

Oxygen Reduction Reaction. For investigation of the ORR activity, the materials were loaded onto glassy carbon electrodes for CV measurements in N_2 and O_2 saturated 0.1 M KOH (Figure 5a). All CVs conducted in Ar-saturated KOH did not show discernible features as compared to the CVs in O_2-saturated KOH, which suggested no significant reactions had occurred. The significant area under the CV plot for all α-MnO_2 materials was indicative of its highly capacitive nature. As soon as O_2 was introduced into the solution, a current from the oxygen reduction reaction was detected. The reduction peak was measured at -0.17 V *vs.* Ag/Ag^+ for undoped α-MnO_2. Samples MnO_2-2.9%Co and MnO_2-7.6%Co, showed a reduction peak at ca. -0.2 V *vs.* Ag/Ag^+ and samples MnO_2-4.8%Ru and MnO_2-9.4%Ru, showed a prominent reduction peak at *ca.* -0.14 V *vs.* Ag/Ag^+. In the supplementary Figure S8, a CV is presented for a potential region where mainly charge storage *via* double-layer capacitance occurred. The charging current was consistent with the measured (BET) surface area (see also supplementary Figure S9, where no carbon additives were used).

The superior performance of the Ru-doped MnO_2 samples was also seen from the results of the rotating disk experiments (Figure 5b,c and Table 2). The onset potential (measured at a current density of 0.1 mA.cm^{-2}) for all MnO_2 based materials, was higher (by < -0.25 V *vs.* Ag/Ag^+) compared to the RuO_2 sample (-0.28 V *vs.* Ag/Ag^+) and lower compared to the Pt/C-reference sample (-0.09 V *vs.* Ag/Ag^+), Table 2. The onset potential of MnO_2 and the Co-based samples was similar and the best performance was measured for samples MnO_2-4.8%Ru and MnO_2-9.4%Ru at 0.12 V *vs.* Ag/Ag^+. The mass transport limiting (saturating) current measured at 0.8 V *vs.* Ag/Ag^+, showed good catalytic activity for all samples (Figure 5b). The Co-doped MnO_2 samples showed lower saturating currents with increasing cobalt content (see also supplementary Figure S10). Ru-based MnO_2 samples showed a saturating current density of -4.77 mA.cm^{-2} for sample MnO_2-9.4%Ru and 4.73 mA.cm^{-2} for the RuO_2 reference sample. However, overall the Pt/C-reference sample showed the highest saturating current density of -5.21 mA.cm^{-2}, whilst MnO_2-9.4%Ru had similar electrochemical oxygen reduction performance.

α-MnO_2 is already known to be a good ORR catalyst in alkaline media. This was also shown by the Koutecky-Levich plots (see calculations and discussions in the supplementary information). The electron transfer number was calculated at -0.7 V *vs.*
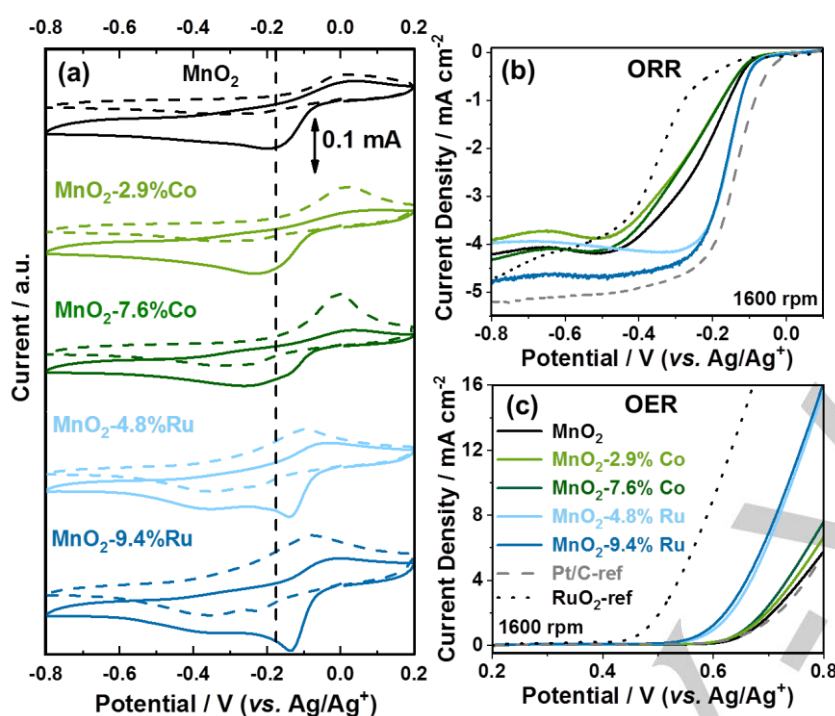
Figure 5. (a) CV curves for all samples on glassy carbon electrodes in O_2-saturated (solid line) and Ar-saturated (dash line) 0.1 M KOH. (b) Rotating-disk voltammograms in O_2-saturated 0.1 M KOH with a sweep rate of 5 mV.s^{-1} for ORR. (c) Rotating-disk voltammograms in 0.1 M KOH with a sweep rate of 5 mV.s^{-1} for OER at a rotating rate of 1600 rpm each.

MnO_2 was lower compared to undoped MnO_2, its full potential was not evaluated in a fair comparison herein. With increasing cobalt dopant concentration, the activity was limited, which is in line with the literature[8a, 10a] and comparable with pure Co_3O_4 (supplementary Figure S10). Ru-doping into α-MnO_2 improved the ORR performance.[31] The Ru-incorporation within the sample (either doping and secondary phase) was expected to increase the electronic conductivity (see supplementary Figure S8 and results from DFT studies) leading to improved ORR performance compared to undoped MnO_2.

Oxygen Evolution Reaction. As mentioned in the introduction, undoped MnO_2 usually shows only moderate performance as an OER catalyst. The OER performance was also investigated *via* LSVs at 1600 rpm (Figure 5c). As expected, the RuO_2 reference was an excellent benchmark material for OER catalysts. The onset potential (at the defined current density of 1 mA.cm^{-2}) was slightly reduced with Co-doping (0.67 and 0.65 V *vs.* Ag/Ag$^+$ for MnO_2 and MnO_2-7.6%Co, respectively). Incorporation of Ru^{4+} into the manganese oxide, decreased the onset potential to 0.59 V *vs.* Ag/Ag$^+$ for the MnO_2-4.8%Ru sample,

which could not quite match the performance of pure undoped RuO_2 (0.48 V *vs.* Ag/Ag$^+$), but exceeded the Pt/C reference material (0.68 V *vs.* Ag/Ag$^+$). Doping of MnO_2 with Co slightly improved the OER performance, although the surface area was lower compared to undoped MnO_2 (while Ru doping drastically shifted the performance towards a better OER catalyst). The superior OER performance of the doped MnO_2 based samples compared to Pt/C reference was further supported by the measured Tafel slope (Figure S13). The Pt/C reference showed a Tafel slope of 102 mV / decade [32], whilst samples MnO_2, MnO_2-7.6%Co and MnO_2-9.4%Ru showed a Tafel slopes of 63, 57 and 62 mV / decade, respectively, in the lower over-potential

Ag/Ag$^+$ and showed a value of *ca.* 4 for the Pt/C-reference, undoped MnO_2, MnO_2-7.6%Co and MnO_2-9.4%Ru samples, suggesting a 4-electron transfer process. The RuO_2 reference sample showed an average transfer number of only 3.4 electrons reflecting its poorer ORR performance compared to the best manganese oxide samples.

Overall, α-MnO_2 is known to be an excellent ORR catalyst,[30] which was further confirmed in the work herein. Co-doping of α-MnO_2 at low concentrations was expected to be beneficial for ORR (see data showing similar ORR activity, despite lower surface area). Considering that the surface area of Co-doped

Table 2. Electrochemical characterizations: (a) onset potential at -0.1 mA cm^{-2} and (b) saturating current at -0.8 V *vs.* Ag/Ag$^+$, which were each obtained from the ORR results in Figure 5b; (c) onset potential at 0.1 mA.cm^{-2} and (d) measured current at 0.8 V *vs.* Ag/Ag$^+$; which were each obtained from the OER results in Figure 5c; (e) potential difference of the onset potentials for ORR and OER.

sample	a $E_{j=-0.1\_ORR}$ / V *vs.* Ag/Ag$^+$	b j_{sat_ORR} / mA cm^{-2} @-0.8 V *vs.* Ag/Ag$^+$	c $E_{j=0.1\_OER}$ / V *vs.* Ag/Ag$^+$	d $j_{0.8\_OER}$ / mA cm^{-2} @0.8 V *vs.* Ag/Ag$^+$	e ΔE / V
MnO_2	-0.16	-4.22	0.67	5.74	0.83
MnO_2-2.9%Co	-0.18	-4.32	0.66	6.63	0.84
MnO_2-7.6%Co	-0.18	-3.91	0.65	7.63	0.83
MnO_2-4.8%Ru	-0.12	-3.97	0.60	15.65	0.72
MnO_2-9.4%Ru	-0.12	-4.77	0.59	16.21	0.71
Pt/C-ref	-0.09	-5.21	0.68	5.61	0.77
RuO_2-ref	-0.28	-4.73	0.48	29.68	0.76

region. The excellent performance of the RuO_2 reference sample was shown with a low slope of only 50 mV / decade.[11a, 33] A decrease of the slope with higher cobalt dopant content has been previously observed for Mn-Co-oxides.[10a]

The main approach of the work herein was to dope transition metal elements (whose corresponding homometallic oxides are known to be excellent OER catalysts) into α-MnO_2 to improve its OER performance. The onset potential was already higher for all doped MnO_2 based materials compared to the Pt/C reference (Figure 5c). The results herein for Co-doped α-MnO_2 are similar to the results of Menezes *et al.*, who saw increased ORR performance with higher Mn content and increased OER performance with higher Co content in mixed manganese cobalt oxides [10a]; see also references.[34] A drastic increase of OER catalyst activity has been shown with Ru incorporation into α-MnO_2. Interestingly, these samples had a similar surface area compared to the undoped α-MnO_2 sample (71.0 $m^2.g^{-1}$); yet the onset potential was reduced and the saturating current was nearly three times higher (Table 2). It was shown elsewhere, that only 5 to 10 at% Ru in MnO_2 can show superior OER performance.[11a, 31a] For the OER reactions herein, each dopant increased the catalytic activity.

One important parameter for ideal bifunctional catalysts for Zn-air batteries is the potential difference of the onset potential for ORR and OER (see the last column in Table 2). A low potential difference should positively improve energy efficiency. Pt/C and RuO_2 reference materials showed an onset potential difference of 0.77 and 0.76 V, respectively. In comparison, potential

differences of 0.83, 0.83 and 0.71 V were observed for undoped MnO_2, MnO_2-7.6%Co and MnO_2-9.4%Ru samples, respectively. Therefore, these three samples were chosen for initial investigations as a bifunctional catalysts in Zn-air batteries (Figure 6a). These tests can be also seen as an indirect investigation of the stability of the materials under basic testing conditions.

Zinc-Air Battery Testing. In Figure 6b, the initial charge/discharge curves for the MnO_2 samples in comparison to the RuO_2 reference and Pt/C reference samples, are presented. For the ORR (discharging), all MnO_2 based materials showed similar discharge potentials of *ca.* 1.28 V *vs.* Zn/Zn^{2+} and the RuO_2 reference material showed a poorer performance of only 1.17 V *vs.* Zn/Zn^{2+}, which is similar to the previous literature results (see Figure 5). The Pt/C reference sample showed a low discharging potential of 1.23 V *vs.* Zn/Zn^{2+}; this sample displayed a decrease in charge potential during the first 50 cycles, which was also observed in literature reports previously[35] and might be related to a surface activation effect. There was a higher difference for the OER (charge) performance between the samples and references. As expected for OER, the RuO_2 reference sample showed the optimum performance (1.93 V *vs.* Zn/Zn^{2+}) followed by MnO_2-9.4%Ru (1.96 V *vs.* Zn/Zn^{2+}), then MnO_2-7.6%Co (2.05 V *vs.* Zn/Zn^{2+}) and finally undoped MnO_2 (2.13 V *vs.* Zn/Zn^{2+}), which is in agreement with the results from Figure 5c. Pt/C reference only showed a charge potential of 2.16 V *vs.* Zn/Zn^{2+}. The overall voltage difference (ΔE) was therefore 0.93, 0.85, 0.77, 0.68 and 0.76 V for Pt/C reference, MnO_2, MnO_2-7.6%Co, MnO_2-9.4%Ru
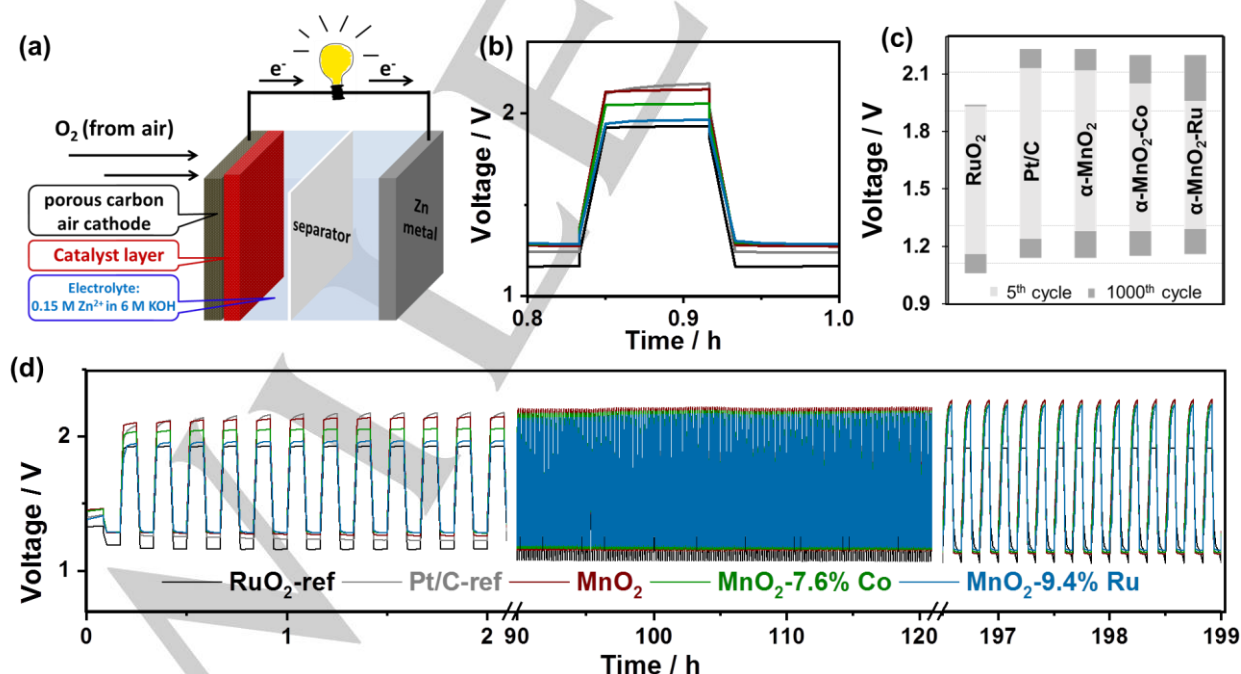

Figure 6. (a) Scheme of a Zn-air battery. (b) First cycles of Zn-air battery testing for samples MnO_2 (red), MnO_2-7.6%Co (green) and MnO_2-9.4%Ru (blue) in comparison to Pt/C reference (grey) and RuO_2 reference (black) at 5 mA.cm^{-2} for 5 min charge/discharge. (c) Over-potentials after various cycles. (d) Overall performance for more than 200 hours of testing.

and RuO$_2$ reference, respectively (Figure 6c).

All materials appeared to be very stable for more than 1200 cycles in the zinc air batteries. After 200 hours of testing, the Pt/C reference and all MnO$_2$ based materials showed similar charge/discharge profiles with a charge potential of 2.25 V *vs.* Zn/Zn^{2+} and a discharge potential of 1.16 V *vs.* Zn/Zn^{2+} (ΔE = 1.09 V). In comparison, the RuO$_2$ reference sample was very stable considering the charge performance with a potential of 1.91 V *vs.* Zn/Zn^{2+} and showed a sloped discharge profile at 1.04 V *vs.* Zn/Zn^{2+} (ΔE = 0.87 V) (Figure 6d).

Conclusions

In the current study, α-MnO$_2$ based materials were synthesized in a single step using a scalable CHFS reactor. Co and Ru atoms were chosen as the potential dopants and the successful doping was shown *via* Rietveld refinements, XAS measurements, and DFT studies. The obtained nanorods appeared to have a specific orientation along the *c*-axis and the dopant position was shown to be the Mn^{4+} position in the MnO$_6$ octahedra. DFT calculations further showed promising characteristics in terms of electronic conductivity for Ru doped in β-MnO$_2$, which should be investigated in future. The materials were investigated as possible bifunctional catalysts in direct comparison to Pt/C and RuO$_2$ reference catalysts. Even though addition of Co$^{2+/3+}$ doping halved the specific surface area, its ORR performance was still similar to the undoped α-MnO$_2$ and its activity during OER was enhanced as compared to the α-MnO$_2$, which was also seen for Zn-air battery testing. Ru doped α-MnO$_2$ showed the most attractive bifunctional catalytic activities among the tested samples, which might be due to improved electronic conductivity during doping. Thus, the use of Co and Ru dopants had affected the physical properties of the host α-MnO$_2$ and influenced the bifunctional catalytic activities of the host catalyst. Furthermore, we have shown that the use of relatively modest amounts of dopants resulted in the significant improvements of the existing bifunctional catalysts.

Experimental Section

Materials

Experimental Details. Potassium permanganate (KMnO$_4$), manganese (II) acetate tetrahydrate [Mn(C$_2$H$_3$O$_2$)$_2$·4H$_2$O] and reagent grade ruthenium(III) chloride hydrate (RuCl$_3$.0.5H$_2$O) were purchased from Sigma-Aldrich (Dorset, U.K.). Cobalt nitrate hexahydrate [Co(NO$_3$)$_2$·6H$_2$O] was purchased from Acros Organics™, Fischer Scientific (Leicestershire, U.K.). The Mn^{7+} precursor and Mn^{2+} precursors were pumped separately before being mixed in a tee-piece; the various dopants were added in with the Mn^{2+} precursor feed as outlined in Supplementary Table 1. All materials were labeled according to the dopant amount from elemental analyses (XRF) rather than the nominal values used in the CHFS precursors; the names used along with the

molar ratios of metal ions used in the precursors (latter in brackets) were as follows; MnO$_2$ (60:38.6 for the Mn^{2+}: Mn^{7+} ratio), sample MnO$_2$-2.9%Co (55:5:44 for the Mn^{2+}: Co^{2+}: Mn^{7+} ratio), sample MnO$_2$-7.6%Co (50:10:44 for the Mn^{2+}: Co^{2+}: Mn^{7+} ratio) , sample MnO$_2$-4.8%Ru (55:5:44 for the Mn^{2+}: Ru^{3+}: Mn^{7+} ratio) and sample MnO$_2$-9.4%Ru (50:10:44 for Mn^{2+}: Ru^{3+}: Mn^{7+}); see supplementary Table S1 and experimental details below for how the various precursors were introduced.

General Synthesis Process

The various α-MnO$_2$ based nanoparticles were synthesized using a laboratory scale CHFS reactor incorporating a patented confined jet mixer (CJM, supplementary Figure S1) [36], and is discussed in more detail in previous publications by the authors [37]. The CJM is a co-current mixing device made from Swagelok™ fittings, where ambient temperature metal salt solutions mix with a low-density supercritical water feed which rapidly forms nanoparticles "in flow". The laboratory scale CHFS process used herein is similar to the pilot scale CHFS process described elsewhere [38] but on *ca.* 1/5 of the scale [38c, 39]. In the lab-scale CHFS process, three identical diaphragm pumps (Primeroyal K, Milton Roy, Pont-Saint-Pierre, France) were used to supply three pressurized (24.1 MPa) feeds. Pump 1 supplied a feed of D.I. water (> 10 MΩ) at a flow rate of 80 mL.min^{-1}, which was then heated to 450 °C in flow using a 7 kW electrical water heater. Pump 2 supplied the low oxidation state precursors at a flow rate of 40 mL.min^{-1} and pump 3 supplied potassium permanganate (Mn^{7+}) solutions at a flow rate of 40 mL.min^{-1}. The feeds from pumps 2 and 3 were combined at room temperature in a dead volume tee-piece. This precursor mixture was then brought into contact with the flow of supercritical water in the CJM co-current mixer under turbulent conditions (Reynolds number of 6939), resulting in a reaction temperature of *ca.* 335 °C (residence time *ca.* 5 s). Thereafter, in the CHFS process, the particle-laden flow was cooled to *ca.* 40°C using a pipe-in-pipe counter-current heat exchanger (cooler), before passing through a back-pressure regulator (BPR) and being collected in a plastic beaker. The resulting nanoparticle-laden slurry was cleaned by allowing the wet solids to settle by gravity before dialyzing them with DI water (<10 MΩ) and then freeze-drying (Virtis Genesis 35XL) by cooling to -60 °C followed by slow heating under vacuum of < 133 Pa over a period of 24 h. The freeze-dried powders were used directly for further analysis.

Materials Characterization

Powder X-ray diffraction (XRD) data of all samples were collected on a Bruker Advance D8 diffractometer (Cu Kα λ = 1.541058 Å) equipped with Ni filter and LynxEye XE energy dispersive 1-D detector over a range of 8-100° 2θ with a step size of 0.02° and collection time of 0.5 s. Variable divergence slit programmed at 10 mm irradiated length were used to maximise signals at the higher 2θ range. Quantitative analysis of the powder X-ray diffraction data was performed on a Bruker Topas 5 in fundamental parameters mode. An initial structural model of α-MnO$_2$ was obtained from ref. [40] with an added oxygen atom (to represent a water molecule) around the centre of the α-MnO$_2$ tunnel at around 0, 0, z (z around ½). For simplicity, we did not model the possible K$^+$ incorporation within the tunnel. Refinement steps started from the most robust parameters (*e.g.* zero error, background, unit cell parameters) progressively to atomic positions and the isotropic thermal factor. Full occupancy of the α-MnO$_2$ was assumed throughout the refinement, but the additional oxygen (representing water molecule) were allowed to relax. Five coefficient Chebyshev polynomials were used to estimate the

background. A separate α-MnO$_2$ phase was added to take into account some degrees of preferred orientation observed in the diffraction data.

X-ray photoelectron spectroscopy (XPS) measurements were collected using a Thermo Scientific K-alpha spectrometer using Al-Kα radiation and a 128-channel position sensitive detector. The XPS spectra were processed using CasaXPS™ software (version 2.3.16) and the binding energy scales calibrated using the adventitious C 1s peak at 285.0 eV. X-ray absorption spectroscopy (XAS) experiment was carried out at XAFCA beamline of the Singapore Synchrotron Light Source under transmission mode [41]. Co K-edge and Mn K-edge were examined. Five scans of each sample were averaged to ensure adequate data quality. The size and morphology of the crystallites were determined by transmission electron microscopy (TEM) using a Jeol JEM 2100 – LaB$_6$ filament. The system was equipped with a Gatan Orius digital camera for digital image capturing. Samples were prepared by briefly dispersing the powder in methanol using ultrasonication and pipetting drops of the dispersed sample onto a 300 mesh copper film grid (Agar Scientific, Stansted, UK). Elemental composition of the samples was determined with an X-ray fluorescence spectrometer (XRF, Rh target, Bruker M4 Tornado). For recording XRF spectra, pellets of the powders were pressed under identical conditions (*ca.* 300 mg, 2 tons of force, 30 s) were used.

Brunauer-Emmett-Teller (BET) surface area analysis (N$_2$ adsorption) of the powders was obtained using a TriStar II PLUS system (Micromeritics, Hertfordshire, UK) and processed using MicroActive™ software. Samples were degassed overnight at 150 °C under flowing nitrogen gas.

Calculations were performed using the periodic density functional theory (DFT) code CRYSTAL14.[42] Electronic exchange and correlation were approximated using the hybrid-exchange functional B3LYP, which is known to give accurate estimates of the band structure of crystalline solids.[43] The atoms were described using triple-valence all-electron Gaussian basis sets with the following forms: Ru (976-311G***), Mn (86-411G**) and O (8-411G*), available from the CRYSTAL14 library (http://www.crystal.unito.it). The DFT exchange and correlation contribution was evaluated by numerical integration over radial and angular coordinates in the unit cell, using Gauss-Legendre and Lebedev schemes respectively. The pruned grid used consisted of 75 radial and 974 angular points. The Coulomb and exchange series were summed and truncated with thresholds of 10^{-7}, 10^{-7}, 10^{-7}, 10^{-7} and 10^{-14} as described previously.[44] Reciprocal space was sampled using a Pack-Monkhorst net,[45] with an 8×8×8 k-point grid. Supercell calculations were performed for Ru-doped α- and β-MnO$_2$, using expansions of 1×1×2 and 2×2×2 of the conventional MnO$_2$ unit cells, respectively, to form 16 cation cells. The self-consistent field (SCF) procedure was performed up to a convergence threshold of ΔE = 10^{-8} Hartree per unit cell. Full geometry optimisations (lattice constants and atomic positions) were performed using the default convergence criteria in CRYSTAL14. Dispersion was estimated using the empirical scheme proposed by Grimme.[46]

Electrochemical Characterization

Cyclic voltammetry (CV), linear sweep voltammetry (LSV) and rotating disk electrode (RDE) measurements were carried out using an Autolab potentiostat/galvanostat (model PGSTAT302N, AUTOLAB, Metrohm, Utrecht, Netherlands) station in a 0.1 M KOH (Merck, Darmstadt, Germany) aqueous electrolyte saturated by O$_2$ or N$_2$ at a scan rate of 5 mV.s^{-1}. Pt foil and Ag/AgCl in 3 M KCl, were used as the counter and reference electrodes, respectively. The working electrode was prepared as follows; (i) dispersing 9.00 mg of the active material with 2.25 mg carbon (Vulcan XC-72) in 3.0 mL of aqueous mixture containing 55 µL

Nafion 117 (5 wt% aqueous solution, Sigma-Aldrich, Dorset, U.K.) *via* sonication for at least 60 min to form homogeneous catalyst ink solution; (ii) applying an appropriate volume of such solution carefully onto a glassy carbon electrode (GC, 5 mm in diameter, Metrohm); (iii) drying it in air to obtain a uniform thin film. The catalyst loadings for all tested materials were ~0.2 mg.cm^{-2}. The reference materials for comparison were RuO$_2$ (Sigma-Aldrich, Milwaukee, USA) and Pt/C (20 wt% Pt, Alfa Aesar, Ward Hill, Massachusetts, USA), which were prepared in an identical manner (thus, the Pt loading in the reference was 16 wt%).

Zn-air batteries were assembled with a custom-made Zn-air cell as described in previous publications.[3b, 3c] 5.25 mg of catalyst was mixed with 1.25 mg carbon and 200 µL Nafion 117 in a solution of 0.9 mL ethanol and 0.9 mL isopropyl alcohol by sonication for 1 h in an ultrasonic bath. This slurry was then cast on a 2.5 × 2.5 cm carbon paper (SGL carbon, Germany) to give an average mass loading of ~1 mg.cm^{-2}. The battery performance was evaluated by continuous discharge-charge experiments performed at ambient temperature conditions in air (oxygen supplied only from the environment, without additional O$_2$) using an alkaline aqueous electrolyte of 6 M KOH (containing 0.15 M ZnCl$_2$) and a polished zinc plate as the negative electrode. The current density of 5 mA.cm^{-2} used for the battery test was normalized by geometric surface area of the catalyst film and applied for 5 min per charge or discharge.

References

[1]   M. K. Debe, *Nature* **2012**, *486*, 43-51.
[2]   M. Carmo, D. L. Fritz, J. Mergel, D. Stolten, *International journal of hydrogen energy* **2013**, *38*, 4901-4934.
[3]   aF. Cheng, J. Chen, *Chemical Society Reviews* **2012**, *41*, 2172-2192; bB. Li, Y. Chen, X. Ge, J. Chai, X. Zhang, T. A. Hor, G. Du, Z. Liu, H. Zhang, Y. Zong, *Nanoscale* **2016**, *8*, 5067-5075; cB. Li, X.

Ge, F. W. T. Goh, T. S. A. Hor, D. Geng, G. Du, Z. Liu, J. Zhang, X. Liu, Y. Zong, *Nanoscale* **2015**, *7*, 1830-1838.

[4]   I. Katsounaros, S. Cherevko, A. R. Zeradjanin, K. J. Mayrhofer, *Angewandte Chemie International Edition* **2014**, *53*, 102-121.

[5]   I. C. Man, H. Y. Su, F. Calle‐Vallejo, H. A. Hansen, J. I. Martínez, N. G. Inoglu, J. Kitchin, T. F. Jaramillo, J. K. Nørskov, J. Rossmeisl, *ChemCatChem* **2011**, *3*, 1159-1165.

[6]   aY. Meng, W. Song, H. Huang, Z. Ren, S.-Y. Chen, S. L. Suib, *Journal of the American Chemical Society* **2014**, *136*, 11452-11464; bF. Cheng, Y. Su, J. Liang, Z. Tao, J. Chen, *Chemistry of Materials* **2009**, *22*, 898-905; cP.-C. Li, C.-C. Hu, H. Noda, H. Habazaki, *Journal of Power Sources* **2015**, *298*, 102-113.

[7]   W. Xia, A. Mahmood, Z. Liang, R. Zou, S. Guo, *Angewandte Chemie International Edition* **2016**, *55*, 2650-2676.

[8]   aM. Lehtimäki, H. Hoffmannova, O. Boytsova, Z. Bastl, M. Busch, N. B. Halck, J. Rossmeisl, P. Krtil, *Electrochimica Acta* **2016**, *191*, 452-461; bD. J. Davis, T. N. Lambert, J. A. Vigil, M. A. Rodriguez, M. T. Brumbach, E. N. Coker, S. J. Limmer, *The Journal of Physical Chemistry C* **2014**, *118*, 17342-17350; cT. N. Lambert, J. A. Vigil, S. E. White, C. J. Delker, D. J. Davis, M. Kelly, M. T. Brumbach, M. A. Rodriguez, B. S. Swartzentruber, *The Journal of Physical Chemistry C* **2017**; dE. Pargoletti, G. Cappelletti, A. Minguzzi, S. Rondinini, M. Leoni, M. Marelli, A. Vertova, *Journal of Power Sources* **2016**, *325*, 116-128.

[9]   aY. Liang, Y. Li, H. Wang, J. Zhou, J. Wang, T. Regier, H. Dai, *Nature materials* **2011**, *10*, 780-786; bY. Liang, H. Wang, J. Zhou, Y. Li, J. Wang, T. Regier, H. Dai, *Journal of the American Chemical Society* **2012**, *134*, 3517-3523; cF. Song, X. Hu, *Journal of the American Chemical Society* **2014**, *136*, 16481-16484; dC. Li, X. Han,

F. Cheng, Y. Hu, C. Chen, J. Chen, *Nature communications* **2015**, *6*.

[10]   aP. W. Menezes, A. Indra, N. R. Sahraie, A. Bergmann, P. Strasser, M. Driess, *ChemSusChem* **2015**, *8*, 164-171; bF. Cheng, J. Shen, B. Peng, Y. Pan, Z. Tao, J. Chen, *Nature chemistry* **2011**, *3*, 79-84.

[11]   aM. P. Browne, H. Nolan, G. S. Duesberg, P. E. Colavita, M. E. Lyons, *ACS Catalysis* **2016**, *6*, 2408-2415; bK. Guo, Y. Li, J. Yang, Z. Zou, X. Xue, X. Li, H. Yang, *Journal of Materials Chemistry A* **2014**, *2*, 1509-1514.

[12]   X. Wang, Y. Li, *Chemical Communications* **2002**, 764-765.

[13]   I. D. Johnson, M. Lübke, O. Y. Wu, N. M. Makwana, G. J. Smales, H. U. Islam, R. Y. Dedigama, R. I. Gruar, C. J. Tighe, D. O. Scanlon, *Journal of Power Sources* **2016**, *302*, 410-418.

[14]   J. A. Darr, J. Zhang, N. M. Makwana, X. Weng, *Chemical Reviews* **2017**.

[15]   C. M. Welch, R. G. Compton, *Analytical and bioanalytical chemistry* **2006**, *384*, 601-619.

[16]   aW. Li, R. Zeng, Z. Sun, D. Tian, S. Dou, *Scientific reports* **2014**, *4*, 6641; bW. Li, X. Cui, R. Zeng, G. Du, Z. Sun, R. Zheng, S. P. Ringer, S. X. Dou, *Scientific reports* **2015**, *5*; cX. Hu, S. Zhu, H. Huang, J. Zhang, Y. Xu, *Journal of Crystal Growth* **2016**, *434*, 7-12; dA. Baral, D. P. Das, M. Minakshi, M. K. Ghosh, D. K. Padhi, *ChemistrySelect* **2016**, *1*, 4277-4285; eZ. Li, Y. Ding, Y. Xiong, Q. Yang, Y. Xie, *Chemical communications* **2005**, 918-920; fB. Li, G. Rong, Y. Xie, L. Huang, C. Feng, *Inorganic chemistry* **2006**, *45*, 6404-6410; gH. Pan, Y. Shao, P. Yan, Y. Cheng, K. S. Han, Z. Nie, C. Wang, J. Yang, X. Li, P. Bhattacharya, *Nature Energy* **2016**, *1*, 16039; hY. Duan, Z. Liu, H. Jing, Y. Zhang, S. Li, *Journal of Materials Chemistry* **2012**, *22*, 18291-18299.

[17]   S. Yamamoto, O. Matsuoka, I. Fukada, Y. Ashida, T. Honda, N. Yamamoto, *Journal of Catalysis* **1996**, *159*, 401-409.

[18] Y. Duan, Z. Liu, Y. Zhang, M. Wen, *Journal of Materials Chemistry C* **2013**, *1*, 1990-1994.

[19] M. M. Sundaram, A. Biswal, D. Mitchell, R. Jones, C. Fernandez, *Physical Chemistry Chemical Physics* **2016**, *18*, 4711-4720.

[20] aM. Chigane, M. Ishikawa, *Journal of the Electrochemical Society* **2000**, *147*, 2246-2251; bA. Nelson, J. G. Reynolds, J. W. Roos, *JOURNAL OF VACUUM SCIENCE AND TECHNOLOGY A VACUUMS SURFACES AND FILMS* **2000**, *18*, 1072-1076.

[21] X. Xiang, L. Zhang, H. I. Hima, F. Li, D. G. Evans, *Applied Clay Science* **2009**, *42*, 405-409.

[22] J. C. Dupin, D. Gonbeau, I. Martin-Litas, P. Vinatier, A. Levasseur, *Journal of Electron Spectroscopy and Related Phenomena* **2001**, *120*, 55-65.

[23] D. S. H.-r. X-ray, *Rev. B* **1972**, *5*, 4709-4714.

[24] D. J. Morgan, *Surface and Interface Analysis* **2015**, *47*, 1072-1079.

[25] S. H. Lee, T. W. Kim, D. H. Park, J.-H. Choy, S.-J. Hwang, N. Jiang, S.-E. Park, Y.-H. Lee, *Chemistry of Materials* **2007**, *19*, 5010-5017.

[26] S. Fritsch, J. E. Post, S. L. Suib, A. Navrotsky, *Chemistry of materials* **1998**, *10*, 474-479.

[27] D. A. Kitchaev, H. Peng, Y. Liu, J. Sun, J. P. Perdew, G. Ceder, *Physical Review B* **2016**, *93*, 045132.

[28] Y.-F. Xu, Y. Chen, G.-L. Xu, X.-R. Zhang, Z. Chen, J.-T. Li, L. Huang, K. Amine, S.-G. Sun, *Nano Energy* **2016**, *28*, 63-70.

[29] aX. Weng, J. K. Cockcroft, G. Hyett, M. Vickers, P. Boldrin, C. C. Tang, S. P. Thompson, J. E. Parker, J. C. Knowles, I. Rehman, *Journal of combinatorial chemistry* **2009**, *11*, 829-834; bR. Quesada-Cabrera, X. Weng, G. Hyett, R. J. Clark, X. Z. Wang, J. A. Darr, *ACS combinatorial science* **2013**, *15*, 458-463.

[30] K. A. Stoerzinger, M. Risch, B. Han, Y. Shao-Horn, *ACS Catalysis* **2015**, *5*, 6021-6031.

[31] aA. J. Jeevagan, Y. Suzuki, T. Gunji, G. Saravanan, Y. Irii, T. Tsuda, T. Onobuchi, S. Kaneko, G. Kobayashi, F. Matsumoto, *ECS Transactions* **2014**, *58*, 9-18; bH. Jang, A. Zahoor, J. S. Jeon, P. Kim, Y. S. Lee, K. S. Nahm, *Journal of The Electrochemical Society* **2015**, *162*, A300-A307.

[32] T. An, X. Ge, T. A. Hor, F. T. Goh, D. Geng, G. Du, Y. Zhan, Z. Liu, Y. Zong, *RSC Advances* **2015**, *5*, 75773-75780.

[33] Y.-H. Fang, Z.-P. Liu, *Journal of the American Chemical Society* **2010**, *132*, 18214-18222.

[34] aE. Davari, A. D. Johnson, A. Mittal, M. Xiong, D. G. Ivey, *Electrochimica Acta* **2016**, *211*, 735-743; bX. Liu, M. Park, M. G. Kim, S. Gupta, X. Wang, G. Wu, J. Cho, *Nano Energy* **2016**, *20*, 315-325.

[35] aA. Sumboja, X. Ge, F. Goh, B. Li, D. Geng, T. Hor, Y. Zong, Z. Liu, *ChemPlusChem* **2015**, *80*, 1341-1346; bS. Guo, J. Liu, S. Qiu, Y. Wang, X. Yan, N. Wu, S. Wang, Z. Guo, *Electrochimica Acta* **2016**, *190*, 556-565.

[36] J. Darr, C. J. Tighe, R. Gruar, Google Patents, **2011**.

[37] aJ. A. Darr, M. Poliakoff, *Chemical Reviews* **1999**, *99*, 495-542; bR. I. Gruar, C. J. Tighe, J. A. Darr, *Industrial & Engineering Chemistry Research* **2013**, *52*, 5270-5281.

[38] aM. Chen, C. Y. Ma, T. Mahmud, J. A. Darr, X. Z. Wang, *The Journal of Supercritical Fluids* **2011**, *59*, 131-139; bC. J. Tighe, R. Q. Cabrera, R. I. Gruar, J. A. Darr, *Industrial & Engineering Chemistry Research* **2013**, *52*, 5522-5528; cM. Lübke, I. Johnson, N. M. Makwana, D. Brett, P. Shearing, Z. Liu, J. A. Darr, *Journal of Power Sources* **2015**, *294*, 94-102.

[39] aM. Lübke, A. Sumboja, I. D. Johnson, D. J. Brett, P. R. Shearing, Z. Liu, J. A. Darr, *Electrochimica Acta* **2016**, *192*, 363-369;

bM. Lübke, J. Shin, P. Marchand, D. Brett, P. Shearing, Z. Liu, J. A. Darr, *Journal of Materials Chemistry A* **2015**, *3*, 22908-22914.

[40] N. Kijima, T. Ikeda, K. Oikawa, F. Izumi, Y. Yoshimura, *Journal of Solid State Chemistry* **2004**, *177*, 1258-1267.

[41] Y. Du, Y. Zhu, S. Xi, P. Yang, H. O. Moser, M. B. Breese, A. Borgna, *Journal of synchrotron radiation* **2015**, *22*, 839-843.

[42] R. Dovesi, R. Orlando, A. Erba, C. M. Zicovich‑Wilson, B. Civalleri, S. Casassa, L. Maschio, M. Ferrabone, M. De La Pierre, P. D'Arco, *International Journal of Quantum Chemistry* **2014**, *114*, 1287-1317.

[43] F. Corà, M. Alfredsson, G. Mallia, D. S. Middlemiss, W. C. Mackrodt, R. Dovesi, R. Orlando, in *Principles and Applications of Density Functional Theory in Inorganic Chemistry II*, Springer, **2004**, pp. 171-232.

[44] C. Pisani, R. Dovesi, C. Roetti, in *Hartree-Fock ab initio treatment of crystalline systems*, Springer, **1988**, pp. 1-33.

[45] H. J. Monkhorst, J. D. Pack, *Physical review B* **1976**, *13*, 5188.

[46] S. Grimme, *Journal of computational chemistry* **2006**, *27*, 1787-1799.

Entry for the Table of Contents (Please choose one layout)

Layout 1:

FULL PAPER

Bifunctional catalysts: α-MnO$_2$ can be synthesized *via* a scalable hydrothermal synthesis process. Modification of α-MnO$_2$ with Co and Ru atoms improves the OER catalytic performance. This can help to improve the energy efficiency of zinc air batteries.
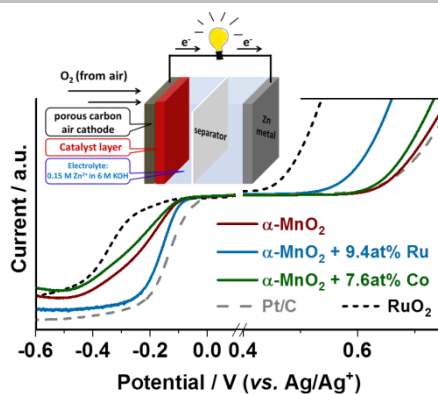
Mechthild Lübke, Afriyanti Sumboja, Liam McCafferty, Ceilidh F. Armer, Albertus D. Handoko, Yonghua Du, Kit McColl, Furio Cora, Dan Brett, Zhaolin Liu, Jawwad A. Darr*

Page No. – Page No.

Transition metal doped α-MnO₂ nanorods as bifunctional catalysts for efficient oxygen reduction and evolution reactions